



Remarkable gas bubble transport driven by capillary pressure in 3D printing-enabled anisotropic structures for efficient hydrogen evolution electrocatalysts

Xiuming Bu^a, Zhengyi Mao^b, Yu Bu^c, Quan Quan^a, You Meng^a, Zhengxun Lai^a, Dong Chen^a, Pengshan Xie^a, Hongkun Li^a, Chuntai Liu^d, Xianying Wang^e, SenPo Yip^f, Jian Lu^{b,c,*}, Johnny C. Ho^{a,f,**}

^a Department of Materials Science and Engineering, City University of Hong Kong, Hong Kong 999077, PR China

^b Department of Mechanical Engineering, City University of Hong Kong, Hong Kong 999077, PR China

^c Centre for Advanced Structural Materials, Shenzhen Research Institute, City University of Hong Kong, Shenzhen 518057, PR China

^d Key Laboratory of Advanced Materials Processing & Mold (Zhengzhou University), Ministry of Education, Zhengzhou 450002, PR China

^e Energy Materials Research Center AG Hydrogen Materials & Devices, CAS Key Laboratory of Materials for Energy Conversion, Shanghai Institute of Ceramics, Chinese Academy of Sciences (SICCAS), Shanghai 200050, PR China

^f Institute for Materials Chemistry and Engineering, Kyushu University, Fukuoka 816-8580, Japan

ARTICLE INFO

Keywords:

Gas bubble transport
Capillary pressure
Additive manufacturing
Anisotropic structures
Hydrogen evolution reaction

ABSTRACT

Additive manufacturing technologies have been proved as a promising method to achieve electrocatalysts with periodic micro-size pores, while the nano-sized interspace of the material structures and their corresponding gas bubbles transfer process are not explored in detail. Herein, we employ the shear force alignment in additive manufacturing to design NiMo-based structures with anisotropic porous channels as electrocatalysts for hydrogen evolution reaction (HER) in seawater. Based on the complementary experimental and theoretical investigation, the unique anisotropic structure not only fully exposes the active sites in the electrolyte, but also facilitates the rapid electrolyte-hydrogen phase conversion during electrochemical reactions. In this case, the obtained 3D electrode exhibits superior electrocatalytic performance and excellent long-term operational stability with an extremely low overpotential of ~ 150 mV at a current density of 500 mA/cm^2 in 1 M KOH seawater. This work will provide a practical scenario for designing highly-efficient HER electrocatalysts.

1. Introduction

Electrochemical water splitting powered by renewable energy sources is capable of producing high purity hydrogen on a large scale with zero carbon emissions, which is considered a promising solution to tackle the energy crisis and associated environmental pollution [1–3]. However, the scarcity, high cost and unsatisfied stability of noble metal catalysts have significantly restricted the development of commercial water electrolyzer systems [4–6]. In this case, it is important to develop the highly-efficient and robust electrocatalysts based on non-noble metals for deployment in industry.

In general, there are two typical strategies employed to improve the activity of electrocatalysts: (i) enhancing the intrinsic activity of single

active site and (ii) increasing the exposed number of active sites [1,7–9]. Until now, various kinds of modification methods have been explored to alter the surface electronic structures of catalysts with the aim to maximize the activity of a single active site, including cation/anion doping, defect manipulation, surface strain modification, and facet and crystal phase engineering [10–12]. At the same time, the electrocatalysts are always prepared in-situ on the three-dimensional (3D) conductive substrate, such as metal foam [13,14], carbon cloth [15,16], and etc. This fabrication scheme would effectively improve the contact between catalysts and current collectors, which is able to reduce the concentration of electrically insulating junction points among the catalyst particles, ultimately leading to the higher electrochemical active surface area (ECSA) and charge carrier transfer efficiency [17,18].

* Corresponding author at: Department of Mechanical Engineering, City University of Hong Kong, Hong Kong 999077, PR China.

** Corresponding author at: Department of Materials Science and Engineering, City University of Hong Kong, Hong Kong 999077, PR China.

E-mail addresses: jianlu@cityu.edu.hk (J. Lu), johnnyho@cityu.edu.hk (J.C. Ho).

<https://doi.org/10.1016/j.apcatb.2022.121995>

Received 5 August 2022; Received in revised form 5 September 2022; Accepted 15 September 2022

Available online 16 September 2022

0926-3373/© 2022 Elsevier B.V. All rights reserved.

Nevertheless, even though there are catalysts developed based on the above two strategies, their electrochemical performance is still from satisfactory. One main limitation may be attributed to the slow detachment process of gas bubbles produced on the catalyst surface [19–21]. It turns out that the gas bubble release from electrodes plays a dictating role in enhancing the efficiency of electrochemical water splitting. Especially for the operating condition of high current density, extensive amounts of gas bubbles are easily formed on the electrodes, blocking large portions of the catalytically active surface area [22]. This blockage would increase the bubble ohmic overpotential and limit the hydrogen production rate. Therefore, taking all these factors into account, the promising candidate for commercially available electrocatalysts should simultaneously provide (i) the capability for manufacturing by a large-scale and low-cost process; (ii) the maximum exposed ECSA in electrolytes; (iii) the proper electronic structure of active sites; (iv) the quick conversion between gas bubbles and electrolytes on the electrode surface.

Recently, for electrochemical applications, 3D printing technologies have been widely employed to design and fabricate hierarchical electrodes with periodic micro-size pores, exhibiting unique physical and mechanical properties [23–25]. Particularly, once the gas bubbles nucleate and grow on the electrode surface during electrochemical reactions, they will rise under the influence of buoyancy in the electrolyte. Compared with the irregular pores randomly scattered in the internal space of commercial 3D substrates, the ordered micron-sized pores in the 3D-printed periodic structure would effectively reduce the frequency of bubble collisions and deformations, thus resulting in a quick bubble release. In any case, the study of gas bubbles dynamics was mostly focused on the pores (usually several hundred micrometers) in the literature, the gas bubble transfer behaviors in the interspace of the material structures (in the order of tens to hundreds of nanometers) was rarely investigated.

Herein, we employ a direct ink writing, one of the most popular additive manufacturing technologies, to fabricate NiMo-based structures with anisotropic porous channels as electrocatalysts for hydrogen evolution reaction (HER) in seawater. The ECSA (geometric area) and the ECSA-specific activity (mass activity per ECSA) of prepared 3D structures are impressively high, demonstrating their effectiveness for contacts between electrocatalysts and electrolytes as well as their advantages for optimizing gas bubble transfer behaviors. The visualization experiments and the computational simulation studies are then performed to reveal the important role of capillary force during gas bubble release and electrolyte phase conversion process. Combined with the electrochemical measurement, it is evident that the 3D-printed electrodes exhibit superior electrocatalytic performance and excellent long-term operational stability with an extremely low overpotential of ~ 150 mV at a current density of 500 mA/cm^2 in 1 M KOH seawater. All these findings would provide valuable insights into the design of highly efficient electrocatalysts through additive manufacturing for future high-purity hydrogen production.

2. Materials and methods

2.1. Preparation of NiMo nanorods

NiMo nanorods were prepared based on our previous reports with a slight modification. Typically, 2.4 g of $\text{NiCl}_2 \cdot 6\text{H}_2\text{O}$ and 2.4 g of $\text{Na}_2\text{MoO}_4 \cdot 2\text{H}_2\text{O}$ were dissolved in 20 mL of distilled water, respectively. Then, the $\text{NiCl}_2 \cdot 6\text{H}_2\text{O}$ solution was added into the $\text{Na}_2\text{MoO}_4 \cdot 2\text{H}_2\text{O}$ solution slowly to form a clear and transparent mixture solution under stirring condition. The mixture solution was next sealed into a 50 mL size of Teflon-lined stainless steel autoclave reactor, which was heated at 140°C for 12 h in an electric oven. After cooling the system to room temperature naturally, the precipitates were gathered and washed several times with ethanol and deionized water by centrifugation, eventually vacuum dried at 60°C overnight.

2.2. Preparation of NiMo powders

Typically, 2.4 g $\text{NiCl}_2 \cdot 6\text{H}_2\text{O}$ and 5.6 g $(\text{NH}_4)_6\text{Mo}_7\text{O}_{24}$ were dissolved in 50 mL distilled water, respectively. Then the $\text{NiCl}_2 \cdot 6\text{H}_2\text{O}$ solution was added into the $(\text{NH}_4)_6\text{Mo}_7\text{O}_{24}$ solution slowly at 80°C under stirring condition. The precipitates were gathered and washed several times with ethanol and deionized water by centrifugation, then vacuum dried at 60°C overnight.

2.3. Preparation of 3D Printed NiMo Electrodes

To start with, the pluronic F127 powder (25 wt%) was mixed with deionized water using a planetary mixer (ARE-310, Thinky) operated at 2000 rpm for 4 min to form the precursor ink, where the ink was then placed at 4°C overnight to have a complete dissolution. Next, the prepared NiMo nanorods were mixed with the F127 precursor ink at a weight ratio of 1:2 by the mixer operated at 2000 rpm for 2 min. After that, the ink was loaded in a syringe and centrifuge at 4000 rpm for 2 min to remove all the air bubbles. The 3D structure was established at room temperature using an extrusion-based 3D printer (BS5.1, GeSIM) with a $600 \mu\text{m}$ nozzle at a printing speed of 8 mm/s, a printing pressure of 120–200 KPa, and a spacing distance of 1 mm. After molding, the obtained 3D bulk materials were left to dry in ambient for 24 h to solidify the printed structure by removing the excess aqueous solvent. The composite was subsequently annealed at 500°C for 2 h with a heating rate of 1°C min^{-1} under air atmosphere followed by reduction treatment under a Ar/H_2 (200 sccm/50 sccm) environment for 2 h with a heating rate of 5°C min^{-1} at 680°C , 740°C and 800°C , respectively. Once the structure was cooled to room temperature, the H_2 feeding was stopped and 10 sccm O_2/Ar (1:9) gas mixture were introduced for 30 min to passivate the surface. The mass of the printed 3D-printed electrocatalyst was determined carefully by the balance. Specifically, the mass of the fabricated 4 layers, 6 layers, and 8 layers 3D-printed NiMo catalyst were 46 mg, 55 mg, and 66 mg, respectively. For comparison, the NiMo powder was treated with the same process, except for no 3D printing process introduced.

2.4. Characterization

The purity and crystalline structure of prepared samples were evaluated by powder X-ray diffraction (XRD) with a scan rate of $0.05^\circ \text{ s}^{-1}$ in a 2θ scan ranging from 20° to 90° using a Bruker D2 Phaser (Bruker, Billerica, MA, USA) instrument equipped with a monochromatic $\text{Cu-K}\alpha$ radiation. The morphology and dimension of obtained 3D electrodes were assessed by a scanning electron microscope (SEM, Phenom Pro, Phenom-World, The Netherlands) with an accelerating voltage of 10 kV and a field-emission SEM (SU-8010, Hitachi, Tokyo, Japan) with an accelerating voltage of 15 kV. Transmission electron microscopy (TEM) and high-resolution (HR) TEM were conducted by a Tecnai G2 F30 (FEI, Hillsboro, OR, USA) using an accelerating voltage of 200 kV. X-ray photoelectron spectroscopy (XPS) was performed with a VG Multilab 2000 (Thermo Fisher Scientific, Waltham, MA, USA) photoelectron spectrometer using a monochromatic $\text{Al-K}\alpha$ radiation under vacuum at a pressure of 2×10^{-6} Pa.

The composition of seawater was measured using an inductively coupled plasma atomic emission spectrometry (PE optima 8000). All the binding energies were referenced to the C1s peak at 284.8 eV of the surface adventitious carbon.

2.5. Electrochemical measurements

For the 3D-printed NiMo electrode, the electrocatalyst was fixed in a home-made conductive support. For the NiMo powder-based electrode, the well-dispersed powder catalyst ink was prepared by ultrasonication with 15 mg of electrocatalyst, 10 μL of distilled water, 30 μL of ethanol, 5 μL of Nafion for 2 h. Then, 5 μL of the catalyst ink was pipetted onto the

glass carbon electrode surface (5 mm in diameter, $S = 0.19625 \text{ cm}^2$). All electrochemical characterization was investigated with a Gamry 300 electrochemical workstation connected with a standard three-electrode configuration under 25°C using a constant temperature bath. The fabricated electrode sample was used as the working electrode. A saturated calomel electrode (SCE) and a carbon rod were employed as the reference electrode and counter electrode, respectively. All the reported potentials were calibrated versus the reversible hydrogen electrode (RHE) using the equation of $E_{\text{RHE}} = E_{\text{SCE}} + (0.2415 + 0.059 \times \text{pH}) \text{ V}$, where E_{RHE} was the potential referred to RHE and E_{SCE} is the measured potential against the SCE reference electrode. The electrochemical activity of the samples towards HER was surveyed in 1 M KOH aqueous solution ($\text{pH} = 14$) and seawater (Kowloon Bay, Hong Kong, $\text{pH} = 13.98$) by linear sweep voltammetry (LSV) at a scan rate of 5 mV s^{-1} . To keep the electrode surface in a relatively stable state, several cyclic voltammetry (CV) cycles were operated before the assessment of electrochemical activity until the hydrogen evolution current showed the unnoticeable change. Unless otherwise mentioned, the voltammograms were recorded with the iR drop compensation automatically on the workstation. Electrochemical impedance spectroscopy (EIS) was conducted at 1.5 V (vs. RHE) over a frequency range of between 0.05 Hz and 100 kHz at 5 mV s^{-1} .

3. Results and discussion

3.1. Preparation and characterization of 3DP NiMoAS and 3DP NiMoIS

In this work, the extrusion-based 3D printing was used to prepare the

NiMo-based electrode with an obvious anisotropic structure, labelled as 3DP NiMoAS (Fig. 1a). The detailed manufacturing process was shown in Fig. S1. In brief, based on our previous work, the multi-gram scale NiMoO_4 nanorods could be synthesized via a simple hydrothermal method, with NiCl_2 and Na_2MoO_4 as the precursors (Fig. S2 and S3) [26]. The anisotropic structure was realized by the shear force inside of the nozzle during the extrusion process [27]. For comparison, the 3D printed NiMo-based electrode with an isotropic structure, labelled as 3DP NiMoIS, was also prepared with $\text{NiMoO}_4 \cdot x\text{H}_2\text{O}$ nanoparticle/F127 as the printing ink (Fig. 1b and Fig. S4). The structural orientation of these printed 3D electrodes was characterized in detail with scanning electron microscopy (SEM). Since the $\text{NiMoO}_4 \cdot x\text{H}_2\text{O}$ nanorods underwent shear-induced alignment during the printing process, the orientation of nanorods was long-range ordered with the assistance of F127 fluid (Fig. 1c and Fig. S5) [27]. Obviously, the 3DP NiMoAS kept the long-range ordered structure under well-controlled processing parameters, where the width of nanorods was around 37 nm, being consistent with the TEM results. Especially, the nanorods were connected with each other under high temperature to form a conductive network, which can significantly reduce the number of electrically insulating junction points [20]. Moreover, this unique structure allowed nearly all electrocatalysts in the internal space to participate in the reaction, being superior to conventional 3D substrates employed to maximize the energy conversion area (such as Ni foam [11], NiFe foam [14], carbon fiber [28], etc.). When the nanorods were replaced with nanoparticles, the disorderly cross-linked network was formed, which was consistent with the previous studies (Fig. 1d) [29]. To further evaluate these anisotropic and isotropic structures, Image-J software was used to visualize the local

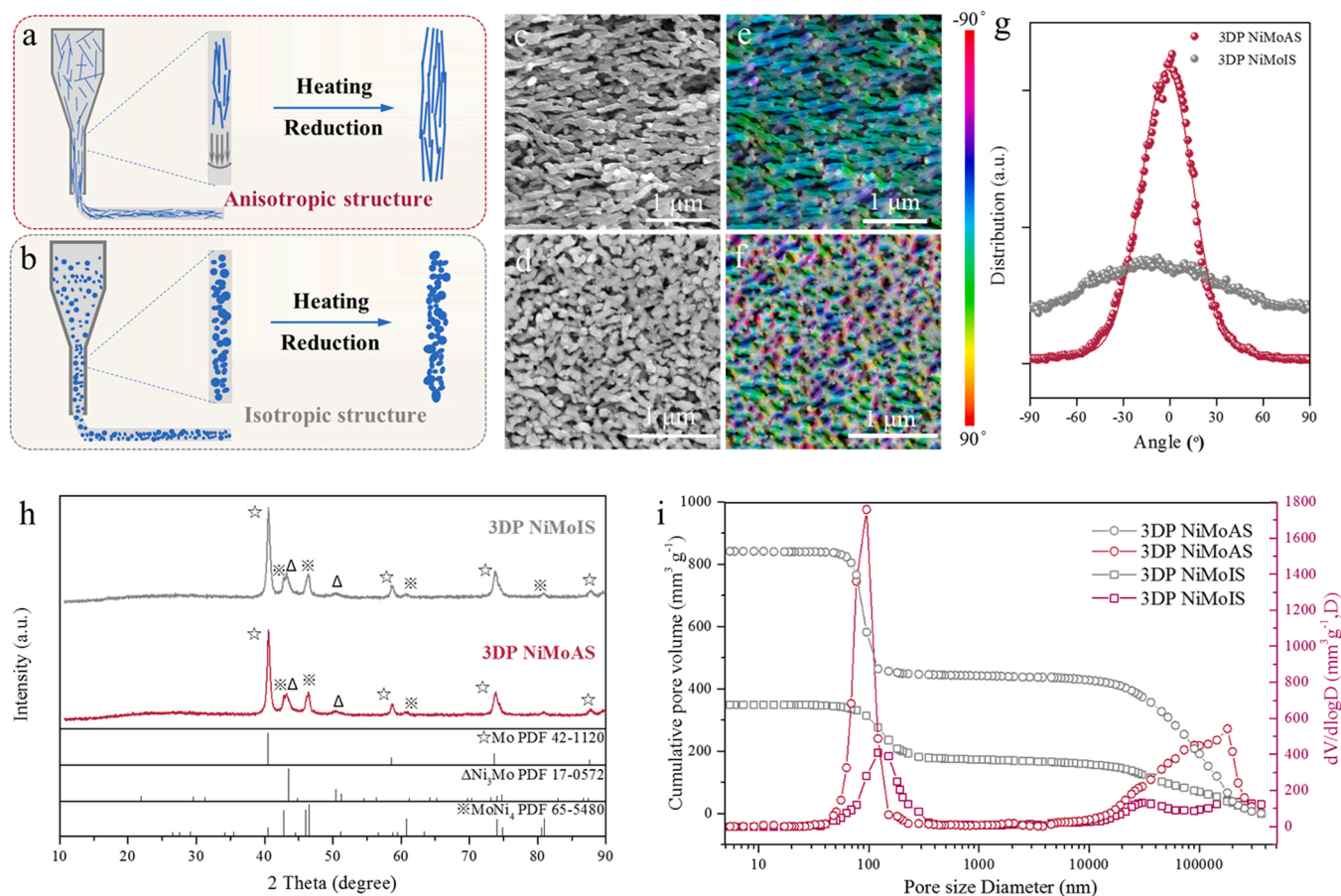


Fig. 1. (a) and (b) were schematic diagrams of the preparation of 3DP NiMoAS and 3DP NiMoIS, respectively. (c) and (d) were their typical SEM images. (e) and (f) were angular space correlation alignment intensity distributions of the 3DP NiMoAS and 3DP NiMoIS, respectively. (g) the orientational parameter S determined from the Image-J software. (h) and (i) were the XRD patterns and pore size distributions of the prepared samples.

orientation of nanorods and nanoparticles (Fig. 1e and 1f). Compared with the isotropic structure, the clear directionality peak at 0° of the anisotropic structure evidently indicated that the nanorods were well oriented by the shear force during printing (Fig. 1g) [30]. The X-ray diffraction (XRD) results revealed that the crystal composition of 3DP NiMoAS and 3DP NiMoIS electrodes both compose of Mo (JCPDS No.42–1120), Ni_3Mo (JCPDS No.17–0572) and MoNi_4 (JCPDS No.65–5480) (Fig. 1h). This finding indicated that the only difference between these two electrodes was the transfer channel orientation. Fig. 1i exhibited the cumulative pore-volume and pore-size distribution curves of the 3DP NiMoAS and 3DP NiMoIS obtained from mercury-intrusion porosimeter method. Obvious sharp peaks were observed in the logarithmic differential pore-volume distribution versus pore size distribution plots, designating the uniform pore size distribution. The pore size of 3DP NiMoAS and 3DP NiMoIS were close to 95.4 nm and 119.6 nm, respectively. The porosity analysis showed the porosity and tortuosity of 3DP NiMoAS and 3DP NiMoIS as 83.8%, 3.2% and 64.0%, 14.2, respectively. Moreover, the total pore volume was $842.2 \text{ mm}^3 \text{ g}^{-1}$ for 3DP NiMoAS, which was significantly higher than that of 3DP NiMoIS with $349.2 \text{ mm}^3 \text{ g}^{-1}$, demonstrating a larger exposed ECSA in the electrolyte.

To demonstrate the rapid absorption and transfer ability of the low tortuous anisotropic pore structure, the absorption performance of the 3DP NiMoAS electrode was conducted and compared with that of 3DP NiMoIS. In Fig. 2a and 2b, five typical digital images showed the electrolyte absorption and transfer behavior of each electrode structure in 1 M KOH (dyed red for easy observation). Firstly, the apparent contact angle was obtained via the Wilhelmy method [22]. It was clear that the apparent contact angle of 3DP NiMoAS ($\sim 33^\circ$) was smaller than the one of 3DP NiMoIS ($\sim 40^\circ$). This result further demonstrated the inconsistencies in the surface morphology and roughness caused by different degrees of orientation between the 3DP NiMoAS and the 3DP NiMoIS. Moreover, the small contact angle ($< 90^\circ$) indicated the electrolyte with a Wenzel state on the surface being easier to penetrate into the porous frame [22]. The Washburn equation could be used to describe the relationship between the liquid absorption height and the contact angle:

$$h^2 = \frac{r\gamma\cos\theta}{2\eta}t$$

where h was the liquid absorption height, r was the electrode radius, γ and η were the surface tension and viscosity of the electrolyte, θ was the

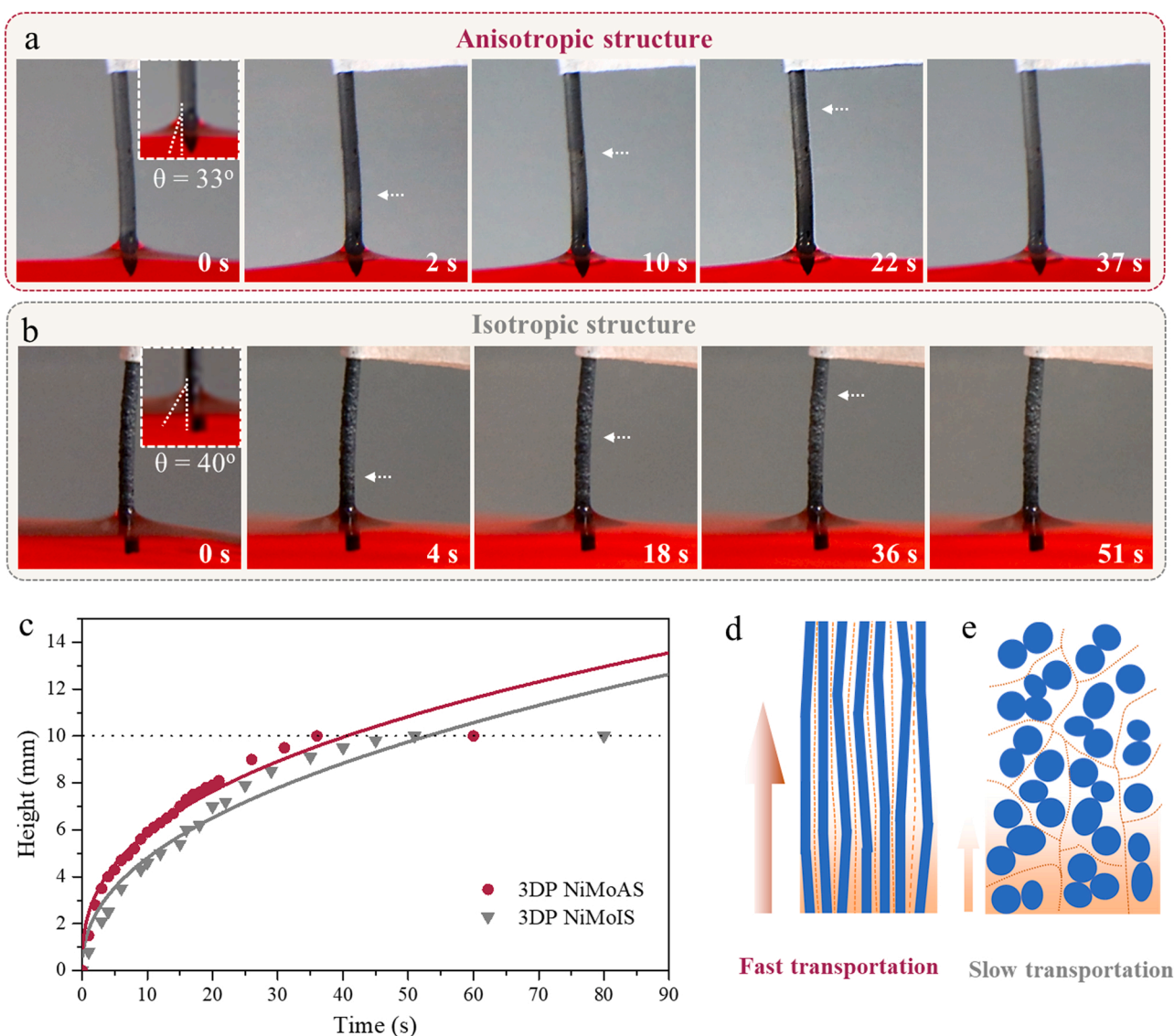


Fig. 2. (a) and (b) were the successive digital photos of KOH liquid absorbing behavior of the 3DP NiMoAS and 3DP NiMoIS, respectively. (c) The height of the absorbed liquid versus time. (d) and (e) were the proposed liquid transfer path in the inner space of the 3DP NiMoAS and 3DP NiMoIS, respectively.

contact angle between the electrode and the electrolyte [31]. Therefore, the 3DP NiMoAS electrode with a smaller contact angle was expected to have a faster absorption speed. As illustrated in Fig. 2c, the profiles of absorption height versus time, recorded and calculated based on the images, further supported the expectation. Based on the above analysis, here, the orientation of transfer channels had a decisive effect on the electrolyte absorption (Fig. 2d and e). Compared with the randomly scattered nanopores in the 3DP NiMoIS electrode, the long-distance ordered channels with low curvature and small nanopore size gave 3DP NiMoAS a large capillary force, which facilitated electrolyte uptake and transfer.

In order to evaluate the effect of orientation on the electrode more intuitively, the gas bubble transport behavior of 3DP NiMoAS and 3DP NiMoIS electrodes was investigated. When the applied potential on the 3DP NiMoAS electrode was -10 mV (vs RHE), gas bubbles appeared at the tip of the electrode, while no gas bubbles could be observed on the electrode surface. With the increasing potential, a small amount of bubbles started to appear on the electrode surface, but a larger number of bubbles was coming out from the tip region (Fig. 3a). The surface was not completely covered by gas bubbles until the applied cathode voltage reached -105 mV (vs RHE). When the voltage continued to increase, the H_2 generation density increased, and some bubbles would escape along the direction perpendicular to the surface. However, once the 3DP NiMoIS electrode was employed as a cathode, an additional increase in the applied voltage (45 mV) was needed to initiate gas bubble detachment on the electrode surface (Fig. 3b). More importantly, even when the cathode voltage reached -185 mV (vs RHE), gas bubbles only detached from the electrode surface rather than the tip region. As displayed in Fig. 3c, the liner sweep curves showed that the 3DP NiMoAS electrode had a better HER performance than that of the 3DP NiMoIS

electrode. It should be noticed that the current density was normalized via specific surface area (Fig. S6). Moreover, based on the electrochemical double-layer capacitance (C_{dl}) values of the electrodes obtained from cyclic voltammetry curves, the 3DP NiMoAS electrode had a similar ECSA with the one of 3DP NiMoIS (Fig. 3d and Fig. S7). The current densities normalized with ECSA could more accurately compare the electrochemical activity of electrocatalysts. The 3DP NiMoAS electrode still exhibited the higher performance as compared with that of 3DP NiMoIS, indicating the transfer channels orientation had a significant influence on the gas bubble transfer dynamic and thus affected the corresponding electrochemical performance (Fig. 3e).

3.2. Proposed gas bubbles movement in the 3DP NiMoAS and 3DP NiMoIS

At the same time, it was important to unveil the relationship between the transfer channel orientation and the electrolyte/gas transport behavior in more detail. In this case, a series of simulations were carried out. Firstly, a 3D visualization of the 3DP NiMoAS structure was constructed based on the SEM images via quarter structure generation set method (Fig. S8). The reconstructed 3DP NiMoAS model was featured with nanoscale anisotropy transfer channels. The flow of electrolyte through the interspace was investigated to visualize the transfer channels, as shown in Fig. 4a. The average electrolyte velocity was 1.8×10^{-4} mm/ms and reached a maximum velocity of 1.4×10^{-4} mm/ms in the center of the channel for a constant pressure difference of 0.1 MPa applied to the flow field (Fig. S9). It was noted that the electrolyte and hydrogen exhibited different transfer behaviors along with the same direction, where the speed in the z-direction (i.e., parallel to the channel) was greater than that in the y-direction (i.e., perpendicular

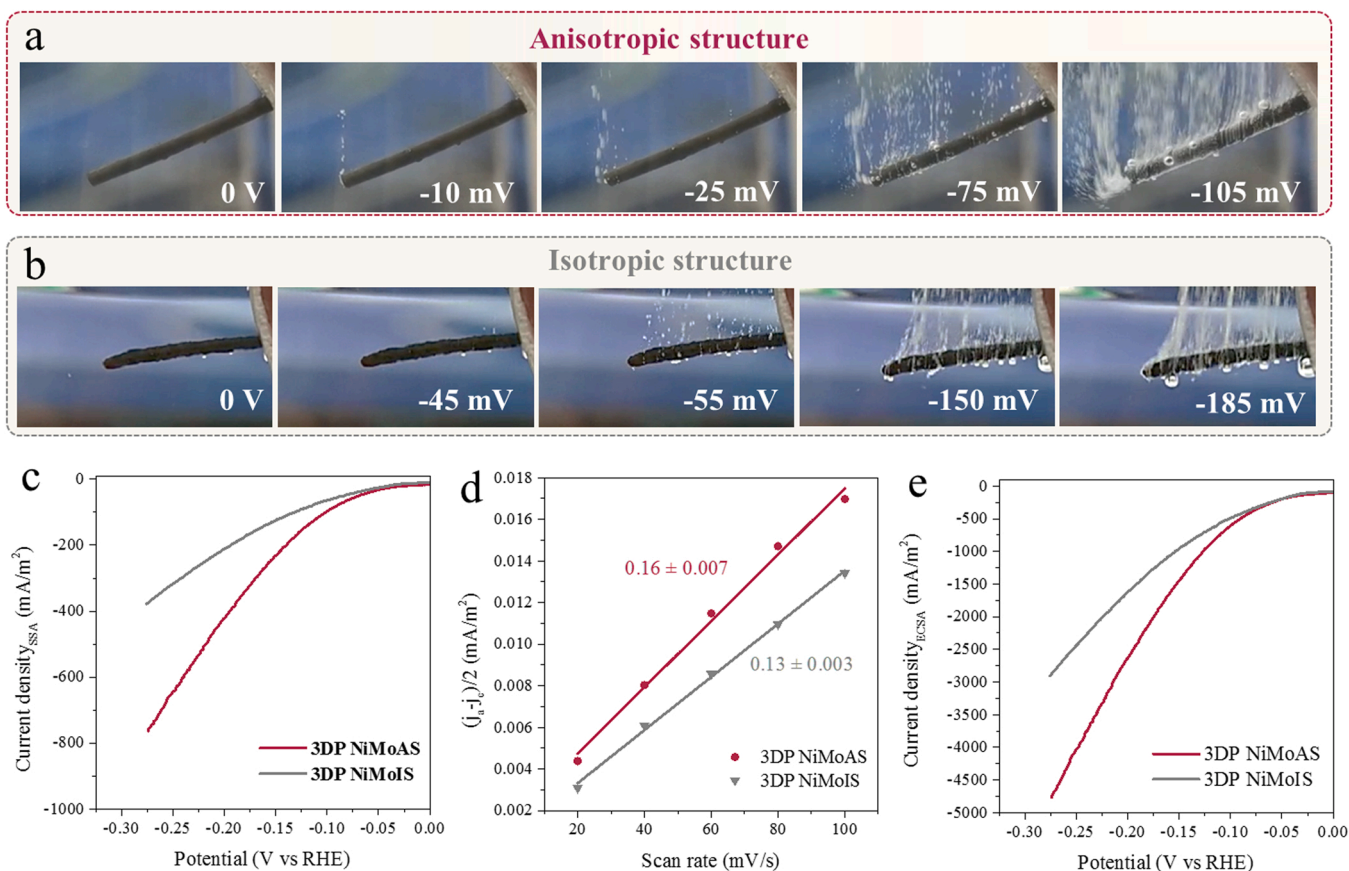


Fig. 3. (a) and (b) were the digital images of 3DP NiMoAS and 3DP NiMoIS electrodes recorded during the HER process. The marked potential was versus RHE. (c) and (d) were the LSV curves and the current density difference ($\Delta j = j_a - j_c$)/2 at -0.85 V plotted against the scan rate; the C_{dl} values for the catalysts were estimated through linear fitting of the plots. (e) LSV curves based on the normalized ECSA.

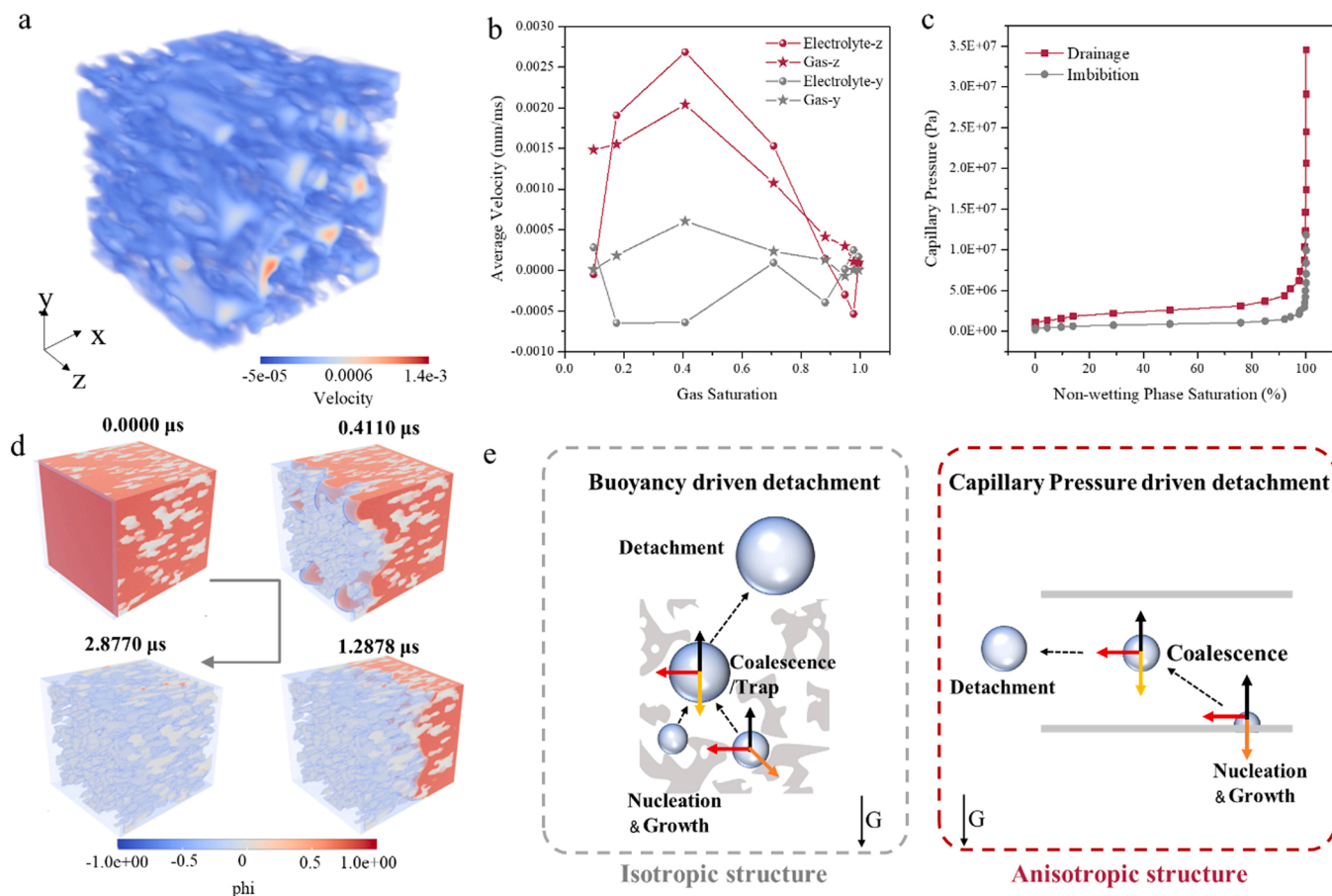


Fig. 4. (a) Simulated electrolyte flow through the 3DP NiMoAS electrode. (b) Electrolyte and H_2 gas bubble transfer velocity in y-axis and z-axis. (c) Capillary pressure versus saturation curves for drainage and imbibition of the electrolyte. (d) Visualization of the flow process of KOH displacing hydrogen, red color: hydrogen gas; blue color: electrolyte; phi was used to distinguish the variable of electrolyte and hydrogen, -1 refers to electrolyte and 1 refers to the hydrogen. (e) Proposed gas bubble transfer pathway in the 3DP NiMoAS and 3DP NiMoIS electrodes. G referred to gravity; orange arrow referred to surface tension force; black arrow referred to buoyancy; red arrow referred to migration force in the horizontal direction; yellow arrow referred to migration force in the vertical direction.

to the channel) (Fig. 4b). In particular, along with the z-direction, the volcano-type relationship was observed between the hydrogen saturation and the gas/electrolyte transfer velocity, in which the electrolyte and gas transfer velocity reached the maximum value of 2.6×10^{-3} mm/ms and 2.0×10^{-3} mm/ms, respectively, for a gas saturation of 0.4. Capillary pressure versus saturation curves for drainage and imbibition were also simulated to investigate the electrolyte (wetting phase)/hydrogen (non-wetting phase) transport behavior (Fig. 4c). Drainage condition described the process of non-wetting phase driving the wetting phase in the transfer channel, while imbibition condition was the opposite, describing the process of wetting phase driving the non-wetting phase [32]. A typical hysteresis between drainage and imbibition was observed, where the capillary pressure needed for pushing hydrogen out of the interspace was smaller than that pushing electrolyte out of the interspace. A capillary pressure of 1.2×10^4 KPa and 3.5×10^4 KPa was then needed to get a full wetting phase saturation and a full non-wetting phase saturation, correspondingly. Fig. 4d provided a more direct observation on the electrolyte permeability process in the existence of hydrogen. The nanosized channel was evidently beneficial for the transport of the wetting phase (Fig. S10).

In fact, for the electrocatalytic process carried out in porous structures, the gas bubble generation and release usually underwent three processes: (i) nucleation and growth on the surface, (ii) coalescence/trapping inside the framework, and (iii) detachment from the porous structure [33]. Specifically, the gas bubbles are first nucleated and grown on the catalyst surface. As the time prolongs, the volume of the bubble increased, and the associated buoyancy (F_b) would increase

accordingly ($F_b = \Delta\rho Vg$, where $\Delta\rho$ was the density difference between gas and liquid, V was the volume of gas bubbles, g was the gravitational acceleration). It should be noticed that the critical size of generated H_2 on the surface is around 5 nm [33]. Thus, when the buoyancy force was greater than the surface tension force at the bubble-catalyst interface, the bubbles would be driven up by buoyancy and then squeezed inside the porous framework, fused, and left the porous catalyst. In this work, in addition to the buoyancy force and the interface surface tension force, the existence of capillary pressure was obviously observed in both isotropic and anisotropic structures. For the 3DP NiMoIS electrode, due to the disordered distribution of irregular nanosized pores and tortuous paths, the frequency of bubble deformation and collision increased even with the participation of capillary pressure here. This increased frequency led to an enhancement of the transfer distance and transfer time, where the increased residence time of non-conductive gas bubbles in the interspace would significantly reduce the ECSA. However, for the 3DP NiMoAS electrode, the influence of capillary pressure on the bubble transport process could not be neglected. Similarly, when the force balance between buoyancy and interface surface tension at the bubble/catalyst interface was broken, bubbles will rise driven by the buoyancy force. During the ascent, the gas bubbles were not only affected by the buoyancy force but also by the electrolyte migration force caused by capillary pressure. It should be noted that the electrolyte migration force was distinctly different from the buoyancy force. The direction of buoyancy was always upward, while the electrolyte migration force had two directions inserted onto the bubbles: parallel to the channel and perpendicular to the channel, which was resulted from

the difference in electrolyte concentration between the surface and the interior of the catalyst rod when the bubbles were generated on the inner surface (Fig. 4e). Therefore, for the 3DP NiMoAS electrode, when bubbles left the catalyst surface, they were subjected to the upward buoyancy force in the electrolyte, electrolyte penetration pressure parallel to the channel, and penetration pressure perpendicular to the channel. Under the combined action of these three forces, hydrogen was pushed out of the structure along the channels.

3.3. Electrochemical performance of 3DPM NiMoAS

After proving the superiority of the anisotropic structure by complementary experimental and stimulation works, a large-area multilayer 3D NiMo-based electrocatalyst assembled by 3DP NiMoAS (3DPM NiMoAS) was printed and corresponding electrochemical measurements

were tested in a three-electrode configuration with 1 M KOH seawater (pH=13.98, Table S1) [34]. In order to optimize the 3D multiscale structure, the electrochemical properties of 3DPM NiMoAS electrocatalysts with different layers (including 4 layers, 6 layers and 8 layers) prepared at 740 °C were first evaluated, as shown in Fig. 5a. It was remarkable that the NiMo-based powder exhibits the highest overpotential at the current density of 100 mA/cm², while the performance of 3DPM NiMoAS electrodes got enhanced substantially. The 3DPM NiMoAS-8 L showed the most outstanding performance among these samples. At only 282 mV, it could provide a geometric current density of ~500 mA/cm². The Tafel slopes of the samples were then obtained, which elucidated the electron transfer kinetics [35]. As depicted in Fig. 5b, the fitted Tafel slope of 3DPM NiMoAS-8 L was 92.7 mV dec⁻¹ when the overpotential was less than 120 mV. This overpotential was smaller than those of 3DPM NiMoAS-4 L (160.8 mV dec⁻¹), 3DPM

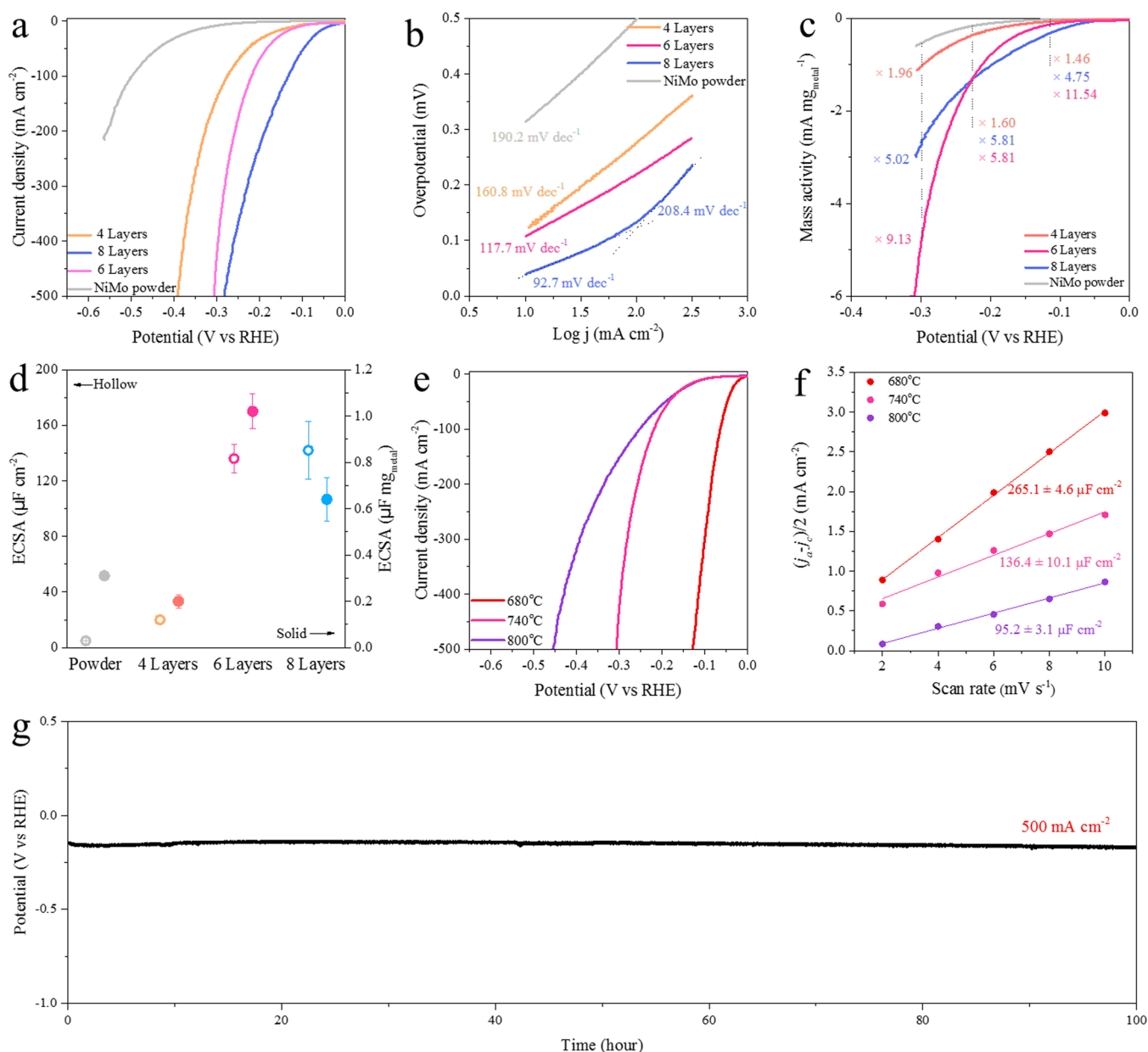


Fig. 5. (a) HER polarization curves obtained with the NiMo foam with 4 layers, 6 layers and 8 layers of catalyst structures. The NiMo powders were prepared at 740 °C characterized in 1 M KOH seawater electrolyte. (b) Corresponding Tafel slopes. (c) Comparison of the mass activity among the samples with different layers and with powders. (d) ECSA values obtained from CV curves. (e) HER polarization curves obtained with the NiMo foam with 6 layers of catalyst structures prepared at 680 °C, 740 °C and 800 °C, respectively. (f) Plots showing the extraction of the C_{dl} values; (g) chronoamperometric test of the NiMo foam with 6 layers of catalyst structures prepared at 680 °C in 1 M KOH seawater with a current density of 500 mA/cm².

NiMoAS-6 L (117.7 mV dec⁻¹) and NiMo powder (190.2 mV dec⁻¹), respectively. While the overpotential was larger than 120 mV, the Tafel slope of 3DPM NiMoAS-8 L approached 208.4 mV dec⁻¹, indicating a low electron transfer process at large current densities, which was attributed to the limited gas bubble movement within the 3D framework as discussed above [20]. Since the 3DPM NiMoAS electrode had a larger surface area, the comparison of current density obtained from geometric area would provide limited information on the superiority of the 3D print technology [36]. Therefore, it was necessary to evaluate the HER performance in terms of the mass activity, where the linear sweeping curves were normalized by metal loading amount. As illustrated in Fig. 5c, the highest mass activity among the 3DPM NiMoAS samples was obtained for 3DPM NiMoAS-6 L with the values of 4.7 mA mg⁻¹_{0.3 V}, which corresponded to 9.1 times of the mass activity of NiMo powder (0.5 mA mg⁻¹_{0.30 V}). Moreover, to investigate the ECSA of prepared samples, the electrochemical double layer capacitance was obtained from the CV curves characterized in the non-Faradaic region (Fig. S11) [37]. The summarized results of ECSA-specific geometric area and ECSA-specific mass activity values were presented in Fig. 5d, suggesting that all the 3DPM NiMoAS samples showed the better performance than the powder-based NiMo electrocatalysts. Notably, the ECSA could be affected not only by the mass transport of products formed within the nanostructure but also by their conductivity. In this case, the Nyquist plots of these samples measured at an overpotential of 100 mV were shown in Fig. S12, revealing that the water inside the well-defined nanoscale pores could provide ionic conductance over a short distance in the 3D long-range ordered structure [19]. The results of SEM, digital photograph, XRD and XPS demonstrated the important effect of temperature on the morphology and electronic structure modification of catalysts, with detailed information compiled in Fig. S13-16.

After confirming the 6-layer structure for the maximization of catalytic performance, the HER performance of the 3DPM NiMoAS-6 L prepared with different temperatures was also evaluated in the 1 M KOH seawater (Fig. 5e). Particularly, the overpotential of 3DPM NiMoAS-6 L-680°C was found to be 128 mV when the current density was 500 mA/cm². This overpotential was 179 mV and 327 mV lower than those of the 3DPM NiMoAS-6 L-740°C and 3DPM NiMoAS-6 L-800°C, respectively. The ECSA-specific geometric area in Fig. 5f indicated that the electronic structure of active sites in the electrocatalysts prepared at the lower temperature was more beneficial for the HER process (Fig. S17). However, the electrocatalyst processed at a lower temperature (<680 °C) had poor mechanical property, being unable to solidify into a stable 3D structure (Fig. S18). We further investigated the stability of 3DPM NiMoAS-6L-680°C under electrocatalytic operation, where a long-term CV test was performed at 500 mV s⁻¹. There was no obvious degradation observed for electrolysis even after a long period of 100 h, suggesting the technological potential of employing these robust catalysts over a long time for electrochemical applications (Fig. 5g).

4. Conclusions

In summary, we take advantages of the shear induced alignments of 3D printing technology to prepare the NiMo-based electrocatalysts with anisotropic structures. Based on the complementary experimental and theoretical investigation, the unique anisotropic structure not only fully exposes the active sites in the electrolyte, but also facilitates the rapid electrolyte-hydrogen phase conversion during electrochemical reactions. It is impressive that the obtained 3D electrode exhibits superior electrocatalytic performance and excellent long-term operational stability with an extremely low overpotential of ~150 mV at a current density of 500 mA/cm² in 1 M KOH seawater. These results will provide important insights into the design of highly-efficient HER electrocatalysts through additive manufacturing to develop hydrogen energy in the future.

CRediT authorship contribution statement

Johnny C. Ho and Jian Lu conceived the project and designed the experiments. Xiuming Bu, Zhengyi Mao, and Yu Bu prepared the material and performed electrochemical measurements. Quan Quan, You Meng, and Zhengxun Lai conducted the theoretical calculations. Dong Chen and Pengshan Xie performed the SEM, TEM imaging, and EDS mapping. Hongkun Li carried out the liquid absorption experiment. Chuntai Liu, Xianying Wang, and SenPo Yip wrote the manuscript. Xiuming Bu, Zhengyi Mao, and Yu Bu contributed equally to this work.

Declaration of Competing Interest

The authors declare that they have no known competing financial interests or personal relationships that could have appeared to influence the work reported in this paper.

Data Availability

Data will be made available on request.

Acknowledgements

This work is supported by the Environment and Conservation Fund of Hong Kong SAR, China (No. ECF 2020-13), the City University of Hong Kong (Project No. 9667227), and the Foshan Innovative and Entrepreneurial Research Team Program (No. 2018IT100031).

Appendix A. Supporting information

Supplementary data associated with this article can be found in the online version at doi:10.1016/j.apcatb.2022.121995.

References

- [1] Z.W. Seh, J. Kibsgaard, C.F. Dickens, I. Chorkendorff, J.K. Nørskov, T.F. Jaramillo, Combining theory and experiment in electrocatalysis: Insights into materials design, *Science* 355 (2017) 146–158.
- [2] S. Dresp, F. Dionigi, M. Klingenhof, P. Strasser, Direct electrolytic splitting of seawater: opportunities and challenges, *ACS Energy Lett.* 4 (2019) 933–942.
- [3] M.S. Faber, S. Jin, Environmental science their nanostructures for energy conversion applications, *Energy Environ. Sci.* 7 (2014) 3219–3343.
- [4] J.A. Turner, Sustainable hydrogen production processes, *Science* 305 (2017) 972–975.
- [5] X. Zou, Y. Zhang, Noble metal-free hydrogen evolution catalysts for water splitting, *Chem. Soc. Rev.* 44 (2015) 5148–5180.
- [6] D.J. Nocum, J. Robinson, H. Yang, Z. Yang, Z. Han, D. Chu, C. Chen, X. Xie, L. Shang, T. Zhang, Highly dispersed platinum deposited on nitrogen-doped vertical graphene array for efficient electrochemical hydrogen evolution Highly dispersed platinum deposited on nitrogen-doped vertical graphene array for efficient electrochemical hydrogen evolution, *2D Mater.* 9 (2022) 045011–045018.
- [7] J. Kang, X. Qiu, Q. Hu, J. Zhong, X. Gao, R. Huang, C. Wan, L.M. Liu, X. Duan, L. Guo, Valence oscillation and dynamic active sites in monolayer NiCo hydroxides for water oxidation, *Nat. Catal.* 4 (2021) 1050–1058.
- [8] Z.J. Zhao, S. Liu, S. Zha, D. Cheng, F. Studt, G. Henkelman, J. Gong, Theory-guided design of catalytic materials using scaling relationships and reactivity descriptors, *Nat. Rev. Mater.* 4 (2019) 792–804.
- [9] Y. Chang, J. Chen, J. Jia, X. Hu, H. Yang, M. Jia, Z. Wen, The fluorine-doped and defects engineered carbon nanosheets as advanced electrocatalysts for oxygen electroreduction, *Appl. Catal. B Environ.* 284 (2021) 119721–119730.
- [10] X. Bu, Y. Li, J.C. Ho, Efficient and stable electrocatalysts for water splitting, *MRS Bull.* 45 (2020) 531–538.
- [11] Z. Cai, X. Bu, P. Wang, J.C. Ho, J. Yang, X. Wang, Recent advances in layered double hydroxide electrocatalysts for the oxygen evolution reaction, *J. Mater. Chem. A* 7 (2019) 5069–5089.
- [12] L. Peng, C. Wang, Q. Wang, R. Shi, T. Zhang, G.I.N. Waterhouse, Rationally designed Ni-Ni₃S₂ interfaces for efficient overall water electrolysis, *Adv. Energy Sustain. Res.* 2 (2021) 2100078–2100085.
- [13] Z. Cai, X. Bu, P. Wang, W. Su, R. Wei, J.C. Ho, J. Yang, X. Wang, Simple and cost effective fabrication of 3D porous core-shell Ni nanochains@NiFe layered double hydroxide nanosheet bifunctional electrocatalysts for overall water splitting, *J. Mater. Chem. A* 7 (2019) 21722–21729.

- [14] X. Bu, R. Wei, W. Gao, C. Lan, J.C. Ho, A unique sandwich structure of CoMnP/Ni₂P/NiFe electrocatalyst for highly efficient overall water splitting, *J. Mater. Chem. A* 7 (2019) 12325–12332.
- [15] V. Vij, S. Sultan, A.M. Harzandi, A. Meena, J.N. Tiwari, W.G. Lee, T. Yoon, K. S. Kim, Nickel-based electrocatalysts for energy-related applications: Oxygen reduction, oxygen evolution, and hydrogen evolution reactions, *ACS Catal.* 7 (2017) 7196–7225.
- [16] C. Hu, Q. Ma, S.F. Hung, Z.N. Chen, D. Ou, B. Ren, H.M. Chen, G. Fu, N. Zheng, In situ electrochemical production of ultrathin nickel nanosheets for hydrogen evolution electrocatalysis, *Chem* 3 (2017) 122–133.
- [17] T. Tang, W.J. Jiang, S. Niu, N. Liu, H. Luo, Y.Y. Chen, S.F. Jin, F. Gao, L.J. Wan, J. S. Hu, Electronic and morphological dual modulation of cobalt carbonate hydroxides by Mn doping toward highly efficient and stable bifunctional electrocatalysts for overall water splitting, *J. Am. Chem. Soc.* 139 (2017) 8320–8328.
- [18] L. Yu, H. Zhou, J. Sun, F. Qin, F. Yu, J. Bao, Y. Yu, S. Chen, Z. Ren, Cu nanowires shelled with NiFe layered double hydroxide nanosheets as bifunctional electrocatalysts for overall water splitting, *Energy Environ. Sci.* 10 (2017) 1820–1827.
- [19] Y.J. Kim, A. Lim, J.M. Kim, D. Lim, K.H. Chae, E.N. Cho, H.J. Han, K.U. Jeon, M. Kim, G.H. Lee, G.R. Lee, H.S. Ahn, H.S. Park, H. Kim, J.Y. Kim, Y.S. Jung, Highly efficient oxygen evolution reaction via facile bubble transport realized by three-dimensionally stack-printed catalysts, *Nat. Commun.* 11 (2020) 1–11.
- [20] T. Kou, S. Wang, R. Shi, T. Zhang, S. Chiovoloni, J.Q. Lu, W. Chen, M.A. Worsley, B. C. Wood, S.E. Baker, E.B. Duoss, R. Wu, C. Zhu, Y. Li, Periodic porous 3D electrodes mitigate gas bubble traffic during alkaline water electrolysis at high current densities, *Adv. Energy Mater.* 10 (2020) 2002955–2002966.
- [21] L. Shang, Y. Zhao, X.Y. Kong, R. Shi, G.I.N. Waterhouse, L. Wen, T. Zhang, Underwater superaerophobic Ni nanoparticle-decorated nickel–molybdenum nitride nanowire arrays for hydrogen evolution in neutral media, *Nano Energy* 78 (2020) 105375–105382.
- [22] R. Iwata, L. Zhang, K.L. Wilke, S. Gong, M. He, B.M. Gallant, E.N. Wang, Bubble growth and departure modes on wettable/non-wettable porous foams in alkaline water splitting, *Joule* 5 (2021) 887–900.
- [23] C.Y. Lee, A.C. Taylor, A. Nattestad, S. Beirne, G.G. Wallace, 3D printing for electrocatalytic applications, *Joule* 3 (2019) 1835–1849.
- [24] X. Aebly, A. Poulin, G. Siqueira, M.K. Hausmann, G. Nyström, Fully 3D printed and disposable paper supercapacitors, *Adv. Mater.* 33 (2021) 2101328–2101337.
- [25] J. Cai, J. Jin, Z. Fan, C. Li, Z. Shi, J. Sun, Z. Liu, 3D printing of a V₈C₇–VO₂ bifunctional scaffold as an effective polysulfide immobilizer and lithium stabilizer for Li–S batteries, *Adv. Mater.* 32 (2020).
- [26] M. Fang, W. Gao, G. Dong, Z. Xia, S.P. Yip, Y. Qin, Y. Qu, J.C. Ho, Hierarchical NiMo-based 3D electrocatalysts for highly-efficient hydrogen evolution in alkaline conditions, *Nano Energy* 27 (2016) 247–254.
- [27] A. Sydney Gladman, E.A. Matsumoto, R.G. Nuzzo, L. Mahadevan, J.A. Lewis, Biomimetic 4D printing, *Nat. Mater.* (2016) 413–418.
- [28] X. Zhou, J. Jiang, T. Ding, J. Zhang, B. Pan, J. Zuo, Q. Yang, Fast colloidal synthesis of scalable Mo-rich hierarchical ultrathin MoSe₂-xnanosheets for high-performance hydrogen evolution, *Nanoscale* 6 (2014) 11046–11051.
- [29] G.J.H. Lim, Z. Lyu, X. Zhang, J.J. Koh, Y. Zhang, C. He, S. Adams, J. Wang, J. Ding, Robust pure copper framework by extrusion 3D printing for advanced lithium metal anodes, *J. Mater. Chem. A* 8 (2020) 9058–9067.
- [30] Q.X. Chen, Y.H. Liu, X.Z. Qi, J.W. Liu, H.J. Jiang, J.L. Wang, Z. He, X.F. Ren, Z. H. Hou, S.H. Yu, Ordered nanostructure enhances electrocatalytic performance by directional micro-electric field, *J. Am. Chem. Soc.* 141 (2019) 10729–10735.
- [31] Y. Cui, Y. Wang, Z. Shao, A. Mao, W. Gao, H. Bai, Smart sponge for fast liquid absorption and thermal responsive self-squeezing, *Adv. Mater.* 32 (2020) 1908249–1908258.
- [32] F. Razmjooei, T. Morawietz, E. Taghizadeh, E. Hadjixenophontos, L. Mues, M. Gerle, B.D. Wood, C. Harms, A.S. Gago, S.A. Ansar, K.A. Friedrich, Increasing the performance of an anion-exchange membrane electrolyzer operating in pure water with a nickel-based microporous layer, *Joule* 5 (2021) 1776–1799.
- [33] Y.A. Perez Sirkin, E.D. Gadea, D.A. Scherlis, V. Molinero, Mechanisms of nucleation and stationary states of electrochemically generated nanobubbles, *J. Am. Chem. Soc.* 141 (2019) 10801–10811.
- [34] H. Jin, X. Liu, A. Vasileff, Y. Jiao, Y. Zhao, Y. Zheng, S.Z. Qiao, Single-crystal nitrogen-rich two-dimensional Mo₅N₆ nanosheets for efficient and stable seawater splitting, *ACS Nano* 12 (2018) 12761–12769.
- [35] R. Wei, X. Bu, W. Gao, R.A.B. Villaos, G. MacAm, Z.Q. Huang, C. Lan, F.C. Chuang, Y. Qu, J.C. Ho, Engineering surface structure of spinel oxides via high-valent vanadium doping for remarkably enhanced electrocatalytic oxygen evolution reaction, *ACS Appl. Mater. Interfaces* 11 (2019) 33012–33021.
- [36] S. Sun, H. Li, Z.J. Xu, Impact of surface area in evaluation of catalyst activity, *Joule* 2 (2018) 1024–1027.
- [37] O.S.G.P. Soares, J.J.M. Órfão, M.F.R. Pereira, Bimetallic catalysts supported on activated carbon for the nitrate reduction in water: Optimization of catalysts composition, *Appl. Catal. B Environ.* 91 (2009) 441–448.